Carrier-envelope-phase control of asymmetries in the multiphoton ionization of xenon atoms by ultrashort bichromatic fields

S. Kerbstadt, D. Pengel, L. Englert, T. Bayer, and M. Wollenhaupt[*]

Carl von Ossietzky Universität Oldenburg, Institut für Physik, Carl-von-Ossietzky-Straße 9-11, D-26129 Oldenburg Germany

We report on bichromatic multiphoton ionization of xenon atoms (Xe) to demonstrate carrier-envelope-phase (CEP) control of lateral asymmetries in the photoelectron momentum distribution. In the experiments, we employ a $4f$ polarization pulse shaper to sculpture bichromatic fields with commensurable center frequencies $\omega_1 : \omega_2 = 7 : 8$ from an over-octave-spanning CEP-stable white light supercontinuum by spectral amplitude and phase modulation. The bichromatic fields are spectrally tailored to induce controlled interferences of 7- vs 8-photon quantum pathways in the $5P_{3/2}$ ionization continuum of Xe. The CEP sensitivity of the asymmetric final-state wave function arises from coherent superposition of continuum states with opposite parity. Our results demonstrate that shaper-generated bichromatic fields with tailored center frequency ratio are a suitable tool to localize CEP-sensitive asymmetries in a specific photoelectron kinetic-energy window.

I. INTRODUCTION

Coherent control of ultrafast electronic processes is based on the phase-sensitive interaction of light and matter at the quantum level. The underlying physical principle is light-induced interference of multiple pathways between the initial and the predefined target state of a quantum system [1]. When all routes lead to the same target state, adjustment of their relative phases permits control of the amplitude of the corresponding wave function and, hence, manipulation of the yield of the corresponding quantum process. Full three-dimensional (3D) control of quantum processes is achieved by exploiting the spatial properties and the angular momenta of the electronic wave functions involved. Driving the system along different routes to continuum states of the same energy but different symmetries (e.g., opposite parity) will, in general, yield an asymmetric target wave function. The spatial asymmetry of this superposition is sensitive to the relative phase between its constituents, which provides the basis to coherently control the directionality of laser-driven quantum dynamics. In recent years, different approaches to induce spatial asymmetries in the target wave function of photoexcited quantum systems have been established. For example, phase-stable few-cycle femtosecond laser pulses have been employed to steer photo-electron wave packets from strong-field ionization of atoms [2–5] and nanometric structures [6–9], control charge localizations in the dissociative ionization of molecules [10–12], and manipulate photocurrents in dielectrics [13] and graphene monolayers [14]. Even before few-cycle laser pulses were available, bichromatic laser fields were used to manipulate the directionality of light-induced quantum processes. In particular, $(\omega : 2\omega)$ fields have been employed in numerous applications, e.g., to steer the photoelectron emission from atoms [15–18], molecules [19–21], and nanostructures [22,23] and to manipulate photocurrents in semiconductors [24,25]

and metals [26]. While the shape of few-cycle laser electric fields is controlled by the carrier-envelope phase (CEP) [27], bichromatic laser pulses depend on both the CEP and the relative phase between the two colors. However, in the traditional scheme to generate $(\omega : 2\omega)$ fields by superposition of a fundamental pulse and its second harmonic, the CEP dependence of subsequent multiphoton excitations cancels [28], rendering the processes CEP insensitive. To combine coherent control strategies based on bichromatic multipath interference and CEP-sensitive ionization, we have developed an alternative approach to generate CEP-stable bichromatic femtosecond laser pulses with variable frequency ratio. We utilize a $4f$ polarization pulse shaper [29,30] to sculpture a bichromatic amplitude profile from an over-octave-spanning CEP-stable white light supercontinuum (WLS) [31,32]. The common-path geometry provides inherent phase stability of the two colors. In addition, by application of individual spectral phase functions to the fields of both colors [33–35], the setup permits the generation of tailored phase-locked bichromatic fields.

In this contribution, we demonstrate coherent control of lateral asymmetries in the photoelectron momentum distribution from multiphoton ionization (MPI) of xenon atoms (Xe) with phase-modulated CEP-stable linearly polarized few-cycle and bichromatic light fields, both generated with the WLS pulse shaping scheme. Employing a velocity map imaging spectrometer (VMIS) for energy- and angle-resolved detection of photoelectrons, we observe pronounced CEP-sensitive asymmetries up to 45% (compared with the CEP average) in the photoemission along the laser polarization direction. We compare results from MPI with phase-modulated CEP-stable few-cycle pulses and tailored bichromatic fields with a frequency ratio of $(7\omega : 8\omega)$, specifically designed to control 7- vs 8-photon interferences at the threshold of the $5P_{3/2}$ ionization continuum of Xe.

We show that shaper-generated bichromatic fields preserve the CEP sensitivity of the MPI process and compare the physical mechanisms of photoionization with phase-modulated CEP-stable few-cycle pulses and tailored bichromatic fields.

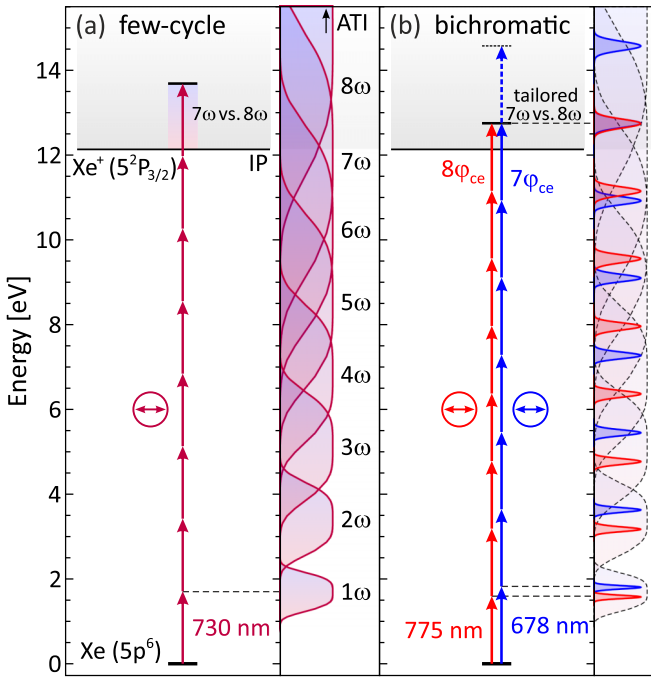*Corresponding author: matthias.wollenhaupt@uni-oldenburg.de

FIG. 1. Multiphoton ionization of Xe using (a) a broadband few-cycle pulse and (b) a bichromatic ($7\omega : 8\omega$) field. The CEP sensitivity of photoelectron wave packets created near the ionization threshold (IP) arises from the interference of 7- and 8-photon ionization pathways.

Our results highlight that the shaper-based bichromatic approach offers full optical control over the involved quantum pathways in terms of the yield via the bichromatic amplitude ratio, and the phase via both the CEP and the relative phase between the two colors. By this means, we are able to localize the CEP-sensitive asymmetries in the target wave packet to a specific photoelectron kinetic-energy window.

In Sec. II, we discuss the physical mechanism of CEP control in the multiphoton regime, introduce the experimental setup and present results on an *in situ* shaper-based pulse characterization procedure. The experimental results on few-cycle and bichromatic CEP control of the MPI from Xe are presented and discussed in Sec. III. Section IV contains a brief conclusion and outlook.

II. EXPERIMENT

In this section, we introduce the physical system and describe the MPI of Xe by phase-modulated few-cycle pulses and shaper-generated ($7\omega : 8\omega$) bichromatic fields (Sec. II A). Subsequently, we describe the experimental procedure including the WLS polarization shaping scheme (Sec. II B), photoelectron imaging techniques (Sec. II C), and our shaper-based *in situ* pulse characterization method (Sec. II D).

A. Physical system

Figure 1 shows the MPI scheme of Xe interacting with a broadband bandwidth-limited few-cycle [Fig. 1(a)] and a bichromatic ($7\omega : 8\omega$) field [Fig. 1(b)], respectively. The right-hand frames schematically display the corresponding normalized Nth order optical spectra. The physical mechanism behind directionality control in the multiphoton regime by the CEP relies on the quantum interference of M- and N-photon excitation pathways leading to final states of the same energy [1,28,36]. Here, M and N are integer numbers of different parity. A perturbative treatment shows [36] that these pathways carry the phases $M\varphi_{ce}$ and $N\varphi_{ce}$, respectively, where φ_{ce} denotes the CEP. According to the dipole selection rules, the (scalar) parity of the process order directly relates to the parity (spatial symmetry) of the final-state wave function. Therefore, the wave functions arising from M- vs N-photon ionization have opposite parity. Their interference results in an asymmetric target wave function with a CEP-dependent spatial asymmetry determined by the relative phase $\Delta\varphi(\omega) = (N - M)\varphi_{ce}$ [4].

In the few-cycle case, as indicated in Fig. 1(a), the ultrabroad bandwidth of the fundamental spectrum induces an energetic overlap of multiple higher-order spectra. In the ionization continuum, this overlap results in a strong mixing of threshold and above-threshold ionization (ATI) channels [4], where only limited optical control can be exerted, e.g., on the mixing ratio by tailoring the fundamental few-cycle field. In addition, interferences occur between different ionization continua associated with the fine structure components $5P_{3/2}$ and $5P_{1/2}$ of the Xe$^+$ ground state, leading to CEP-sensitive intercontinuum interferences. Thus, due to the multitude of coupled ionization pathways leading to the same photoelectron energy, the interpretation of the interference mechanism in few-cycle high-order MPI is generally difficult. An alternative approach to induce controlled M- vs N-photon interferences in a specific photoelectron kinetic-energy window makes use of commensurable bichromatic laser fields with frequency ratio ($M\omega : N\omega$) specifically adapted to the MPI process. Figure 1(b) illustrates the concept for 7- vs 8-photon ionization of Xe by a bichromatic near-infrared ($7\omega : 8\omega$) field. The interfering ionization pathways are determined by the seventh-order spectrum of the blue (i.e., high-frequency) band and the eighth-order spectrum of the red (i.e., low-frequency) band, respectively. Both colors are individually controlled in amplitude, phase, and polarization by spectral shaping of the respective fundamental field [32]. For simplicity, only the single-color pathways are indicated in Fig. 1(b), implying that the two colors do not overlap in time. Otherwise, a manifold of additional pathways arises due to intrapulse frequency mixing [37]. These pathways, however, are strongly interdependent as in the few-cycle case. Moreover, being of the same nonlinear order, their mutual interference within one ionization continuum is CEP insensitive. Therefore, in bichromatic MPI, it is crucial to introduce a sufficiently large time delay between the two colors to prepare the pure M- vs N-photon interference. Next, we briefly introduce the physical quantities to describe and analyze the experimental results in Sec. III. Denoting the released CEP-dependent electron wave packet by $\psi(\boldsymbol{r};\varphi_{ce})$, its probability density is given by $\varrho(\boldsymbol{r};\varphi_{ce}) = |\psi(\boldsymbol{r};\varphi_{ce})|^2$. In the experiment, we measure images of the projected photoelectron distribution (PED) as a function of φ_{ce}. The PED is described by the Abel transform $\mathcal{A}$ of the density along the detector direction (x direction):

$$P(y,z;\varphi_{ce}) = \mathcal{A}[\varrho](y,z;\varphi_{ce}) = \int_{-\infty}^{\infty} \varrho(x,y,z;\varphi_{ce})dx. \quad (1)$$
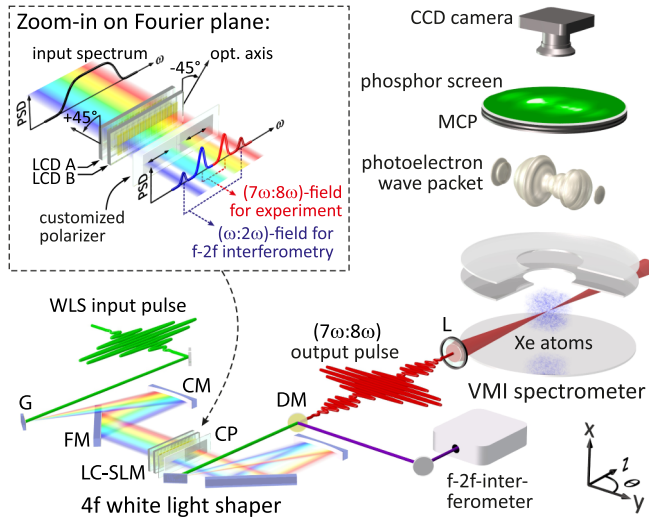
FIG. 2. Experimental setup for CEP control of photoemission from MPI of Xe with shaper-generated bichromatic fields. The WLS pulse is spectrally modulated by using a home-built $4f$ polarization pulse shaper specifically adapted to the ultrabroad WLS. Bichromatic amplitude and phase modulation is implemented with a dual-layer LC-SLM and a p polarizer in the Fourier plane. A multichromatic field is generated, consisting of the $(7\omega : 8\omega)$ field sent to the experiment and an additional $(\omega : 2\omega)$ field, which is split off by using a dichroic mirror to feed a single-shot f-$2f$ interferometer for active CEP stabilization via the amplifier control loop. The CEP-stable $(7\omega : 8\omega)$ field is focused into the VMIS and top projections of the generated asymmetric 3D wave packets are measured as a function of the CEP.

In the following, we switch from the cartesian description of the PED to a representation in polar coordinates $P = P(r, \theta; \varphi_{ce})$ with the planar radius r and the polar angle θ depicted in Fig. 2. Since measurements were performed by using linearly polarized light with the polarization direction parallel to the detector plane, we apply the Abel inversion $\mathcal{A}^{-1}$ to retrieve the section of the photoelectron wave packet in the y-z plane:

$$S(\varepsilon, \theta; \varphi_{ce}) = \mathcal{A}^{-1}[P](\varepsilon, \theta; \varphi_{ce}). \quad (2)$$

Here, ε denotes the photoelectron kinetic energy derived from the energy calibration of the VMIS. The CEP-averaged image

$$\bar{S}(\varepsilon, \theta) = \frac{1}{2\pi} \int_0^{2\pi} S(\varepsilon, \theta; \varphi_{ce}) d\varphi_{ce} \quad (3)$$

serves as a reference to analyze the observed CEP-dependent variation of the photoelectron density. To quantify the photoelectron asymmetry, we calculate the relative difference

$$\Delta(\varepsilon, \theta; \varphi_{ce}) = \frac{S(\varepsilon, \theta; \varphi_{ce}) - \bar{S}(\varepsilon, \theta)}{\bar{S}(\varepsilon, \theta)} \quad (4)$$

between the φ_{ce}-dependent section $S(\varepsilon, \theta; \varphi_{ce})$ and the CEP-average $\bar{S}(\varepsilon, \theta)$, normalized to the average image. The photoelectron asymmetries manifest in the antisymmetric part of Eq. (4) with respect to the laser propagation direction (z direction), given by

$$\Delta_a(\varepsilon, \theta; \varphi_{ce}) = \tfrac{1}{2}[\Delta(\varepsilon, \theta; \varphi_{ce}) - \Delta(\varepsilon, -\theta; \varphi_{ce})]. \quad (5)$$

The resulting 3D data are reduced to two-dimensional energy-resolved CEP-asymmetry maps $A(\varepsilon, \varphi_{ce})$, evaluated around $\theta = 90°$, by integrating over a small angular interval $[70°; 110°]$ in order to focus on direct, i.e., non-rescattered, electrons [38]:

$$A(\varepsilon, \varphi_{ce}) = \int_{70°}^{110°} \Delta_a(\varepsilon, \theta; \varphi_{ce}) \, d\theta. \quad (6)$$

B. CEP-stable white light pulse shaping

The experimental setup is illustrated in Fig. 2. We use a CEP-stabilized *FEMTOLASERS* multipass chirped pulse amplifier (Rainbow 500, Femtopower HR 3kHz CEP, 0.8 mJ pulse energy) to seed a neon-filled hollow-core fiber (absolute gas pressure of 2 bar) and generate a CEP-stable over-octave-spanning WLS. The typical fiber throughput is about 60% resulting in a WLS pulse energy of approximately 0.5 mJ. The WLS pulse is spectrally modulated by using a home-built $4f$ polarization pulse shaper [29,31,33] specifically adapted to the ultrabroad WLS [32]. Spectral phase modulation of the WLS is implemented by a dual-layer liquid crystal spatial light modulator (LC-SLM; *Jenoptik* SLM-640d) situated in the Fourier plane of the $4f$ setup. Initially, the shaper is employed for temporal compression of the WLS. Residual spectral phases are compensated *in situ* by shaper-based adaptive optimization of the photoelectron yield from helium atoms by using an evolutionary algorithm [39,40]. By additional application of polynomial spectral phase masks $\varphi(\omega) = \phi_n(\omega - \omega_0)^n$, where ω_0 denotes the WLS center frequency, we generate linearly chirped ($n = 2$) and Airy-type ($n = 3$) WLS pulses. The former are prototypes for laser pulses with linearly varying instantaneous frequency, while the latter are characterized by an asymmetric temporal amplitude profile and constant instantaneous frequency [35,41]. We note that, in the convention used here, the laser electric field is modulated by the inverse phase $-\varphi(\omega)$ [35]. Bichromatic laser fields are generated by combined amplitude and phase modulation of the WLS by using a p polarizer behind the LC-SLM, as described in detail in Refs. [31,32]. The bichromatic amplitude profile consists of two spectrally separated bands with individually adjustable center frequencies ω_1 and ω_2, amplitudes $\mathcal{A}_1(\omega)$ and $\mathcal{A}_2(\omega)$, bandwidths $\Delta\omega_1$ and $\Delta\omega_2$, and spectral phase functions $\varphi_1(\omega)$ and $\varphi_2(\omega)$. In the experiments described below, we use commensurable center frequencies $\omega_1 = 2.43$ rad/fs (775 nm) and $\omega_2 = 8\omega_1/7 = 2.78$ rad/fs (678 nm) to generate $(7\omega : 8\omega)$ fields [see Figs. 1(b) and 3(a)] required to control the 7- vs 8-photon interferences in the MPI of Xe. By additional application of linear spectral phase masks $\varphi_1(\omega) = \tau\omega$ to the red band, we introduce a time delay τ between the two colors to generate phase-locked bichromatic double-pulse sequences.

To compensate for long-term CEP drifts of the shaped output pulses and, in addition, to control the CEP, a small fraction of the shaper output is split off the main beam to be monitored by a single-shot f-$2f$ interferometer. In the few-cycle case, a beam splitter is used to this end. In the bichromatic case, the spectral f-$2f$ overlap is realized by an additional shaper-generated $(\omega : 2\omega)$ field, with center frequencies $\omega_3 = 2.00$ rad/fs and $\omega_4 = 2\omega_3 = 4.00$ rad/fs, extracted from the wings of the WLS (see inset to Fig. 2). In this case, the beam splitter is replaced by a dichroic mirror to efficiently separate
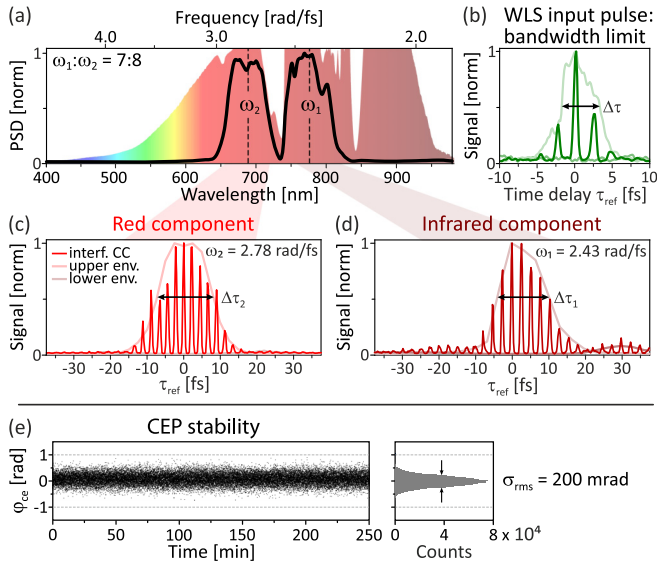
In-situ shaper-based pulse characterization from MPI of Xenon

FIG. 3. Shaper-based *in situ* pulse characterization of the bichromatic ($7\omega : 8\omega$) field. (a) Measured power spectral density (PSD) of the WLS (colored background) and the ($7\omega : 8\omega$) field (black line). (b) Shaper-based CC traces of the WLS input pulse recorded in the interaction region of the VMIS by MPI of Xe. Panels (c) and (d) display CC traces of the red (ω_2) and infrared (ω_1) field, respectively. In the bottom row, a histogram of the CEP measured over 3 h is plotted, revealing a long-term rms of $\sigma_{\text{rms}} = 200$ mrad.

the ($\omega : 2\omega$) monitor field from the ($7\omega : 8\omega$) field sent to the experiment. With the f-$2f$ interferometer output fed back to the CEP control loop of the laser system, we achieve a long-term CEP stability of about 200 mrad root mean square measured over three hours [see histogram in Fig. 3(e)].

C. Photoelectron imaging

In the experiment, we employ photoelectron imaging techniques [42] to measure angular-resolved projections of the photoelectron momentum distribution from MPI of Xe with the shaped laser pulses. The laser pulses are focused into the interaction region of a VMIS by using a spherical mirror with focal length of $f = 250$ mm. The laser beam is attenuated to approximately 10 μJ by a neutral density filter, leading to an estimated peak intensity in the laser focus of $I_0 \approx 4 \times 10^{13}$ W/cm². Xe is supplied by an effusive gas inlet at a pressure of 8×10^{-6} mbar (background pressure 4×10^{-7} mbar). Photoelectron wave packets released during the laser-atom interaction are imaged onto a position-sensitive detector (*Scientific Instruments* S3075-10-I60-PS43-FM) consisting of a dual-layer multichannel plate (MCP) in chevron configuration followed by a phosphor screen. The resulting PEDs $P(r,\theta;\varphi_{ce})$ are recorded by a charge coupled device (CCD) camera (*Lumenera* LW165M) using an exposure time of 200 ms. Each PED was acquired by accumulation of 100 images. The recorded PEDs are Abel inverted by using the PBASEX algorithm [43] and energy-calibrated to retrieve the equatorial section $S(\varepsilon,\theta;\varphi_{ce})$ of the photoelectron wave packet. The energy calibration of the VMIS was performed by using a nar-
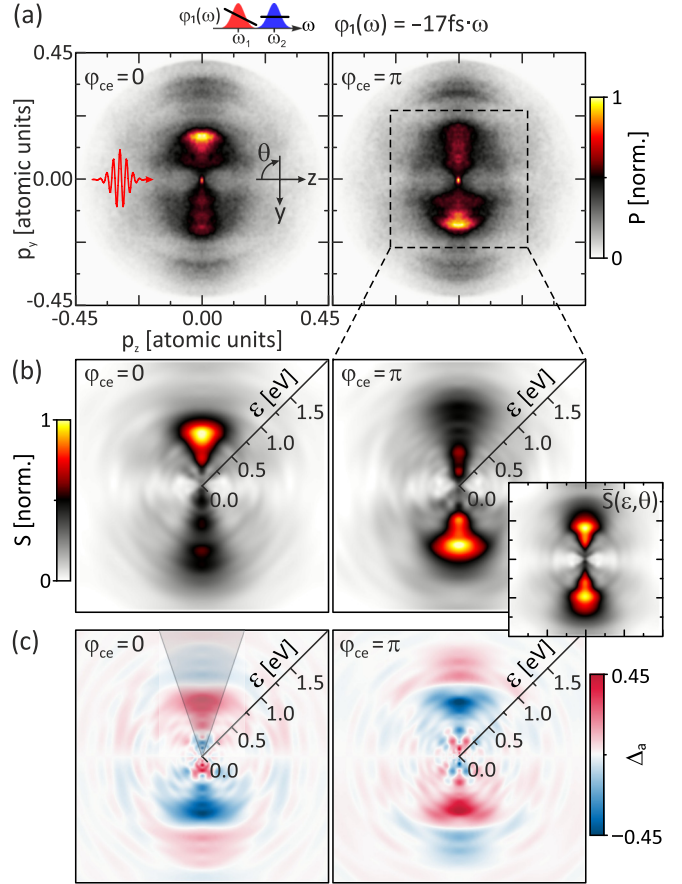

FIG. 4. Calculation of energy-resolved CEP asymmetry maps. (a) Display of raw VMI images $P(r,\theta;\varphi_{ce})$ for $\varphi_{ce} = 0$ (left column) and π (right column), which are Abel-inverted and energy-calibrated to extract the sections $S(\varepsilon,\theta;\varphi)$ through the y-z plane of the 3D electron wave packet shown in panel (b). A zoom-in on the low-energy region [dashed box in panel (a)] is performed to highlight the 7- vs 8-photon interference in the distribution of threshold electrons. The inset shows the CEP-averaged image. (c) Antisymmetric part $\Delta_a(\varepsilon,\theta;\varphi)$ of the normalized difference between each section and the CEP average [cf. Eq. (4)] in the y direction. Angle integration over the gray shaded area yields the photoelectron asymmetry $A(\varepsilon,\varphi_{ce})$.

rowband laser diode tuned to the potassium $5p_{3/2}$ resonance at 404.53 nm, as proposed in Ref. [44]. The lateral photoemission asymmetry as a function of the CEP is obtained by measuring $S(\varepsilon,\theta;\varphi_{ce})$ for various values of φ_{ce} between $-\pi$ and $+\pi$. As described in Sec. II A, the resulting 3D data are analyzed on the basis of two-dimensional (2D) energy-resolved CEP asymmetry maps $A(\varepsilon,\varphi_{ce})$ [see Eq. (6)]. The corresponding procedure is illustrated in Fig. 4 for the example of a bichromatic ($7\omega : 8\omega$) field with a time delay of $\tau = -17$ fs between the two colors. The negative value of the delay indicates that the pulse centered at 775 nm (red with a tilted spectral phase in the sketch at the top of Fig. 4) precedes the field at 678 nm (blue with flat spectral phase in Fig. 4). A pronounced asymmetry in the photoelectron momentum distribution is observed along the laser polarization direction (y direction), which is switched by variation of the CEP from $\varphi_{ce} = 0$ to π.

D. Pulse characterization

The measured bichromatic spectral amplitude profile is shown as a black line in Fig. 3(a) along with the over-octave-spanning WLS (colored background). For temporal pulse characterization, we perform *in situ* shaper-based pulse cross-correlation (CC) measurements in the interaction region of the VMIS [31,32,45]. For this purpose, the pulse shaper mimics an interferometer by splitting off a bandwidth-limited reference pulse via phase and amplitude modulation, in addition to the investigated sample pulse. Both pulses are focused into the VMIS filled with Xe gas. PEDs from MPI of Xe are detected as a function of the time delay τ_{ref} between sample and reference pulse. Integration over all events for each delay leads to low-noise CC traces. As discussed in Refs. [31,32], different shaper-based CC modes are accessible: The interferometric mode, resolving the full carrier oscillation, and the upper and lower pulse envelope, where the carrier oscillation drops out. The detected CC traces reveal the temporal profile of the few-cycle pulse shown in Fig. 3(b). The individual CC traces of the two colors of the bichromatic ($7\omega : 8\omega$) field are depicted in Figs. 3(c) and 3(d). The full width at half maximum (FWHM) is determined to be $\Delta\tau \approx 5$ fs for the few-cycle pulse. The extracted pulse duration of both colors of the ($7\omega : 8\omega$) field is $\Delta\tau_{1,2} \approx 20$ fs.

III. RESULTS AND DISCUSSION

In the experiments, we compare CEP-control of the directional photoemission from MPI of Xe using (*i*) spectrally phase-modulated few-cycle pulses and (*ii*) bichromatic ($7\omega : 8\omega$) fields. The CEP dependence of lateral asymmetries in the photoelectron momentum distributions is analyzed by means of energy-resolved asymmetry maps $A(\varepsilon, \varphi_{ce})$ introduced in Sec. II A. In addition, a polar plot of the CEP average $\bar{S}(\varepsilon, \theta)$ [cf. Eq. (3)] is depicted on top of each asymmetry map in order to facilitate the assignment of observed CEP variations to signal contributions in the photoelectron spectrum. We analyze the CEP dependence of photoelectrons emitted in the field direction, i.e., for an angle $\theta \in [70°, 110°]$, as described in Eq. (6).

A. Phase-modulated few-cycle pulses

We start with the discussion of CEP-sensitive lateral asymmetries from MPI with phase-modulated few-cycle pulses. The recorded asymmetry maps are shown in Fig. 5. Experimental results (top row) are compared with numerical calculations based on spectral interference (SI) in the $5P_{3/2}$ ionization continuum (bottom row). In the case of bandwidth-limited few-cycle pulses shown in Fig. 5(a) (left frame), due to the flat spectral phase $\varphi(\omega) \equiv 0$, the relative phase $\Delta\varphi(\omega) \equiv \varphi_{ce}$ of adjacent ATI and threshold photoelectrons is energy independent.

By application of a quadratic spectral phase modulation $\varphi(\omega) = \phi_2(\omega - \omega_0)^2$ to the fundamental field, the interference fringes shift linearly with increasing energy such that the entire interference pattern obtains a tilt (dashed line), as shown in Fig. 5(b). The physical mechanism behind this tilt was discussed in Ref. [4] in terms of the additional chirp-dependent quantum phase $\Delta\varphi(\omega) = \varphi_{N+1}(\omega) - \varphi_N(\omega)$ of overlapping threshold or ATI channels, which acts as an energy-dependent phase offset to the asymmetry oscillation in the φ_{ce} direction. Within the SI model, $\varphi_N(\omega)$ is determined by the phase of the
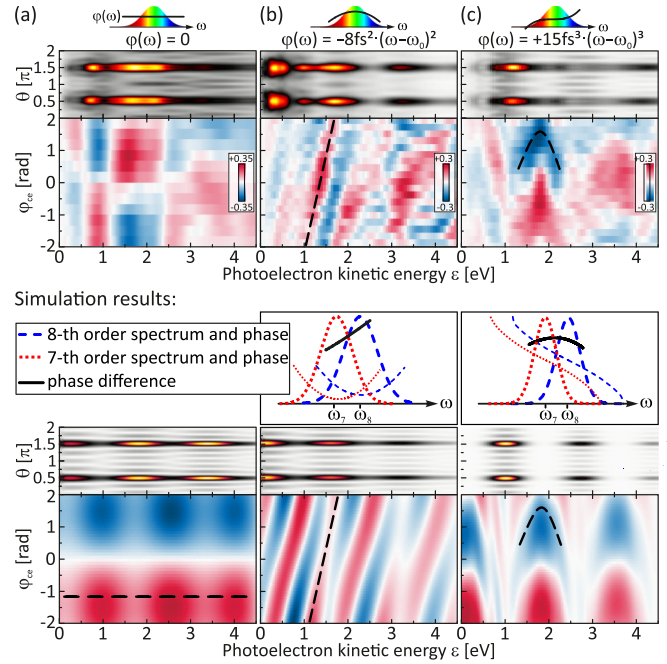

FIG. 5. Phase-sensitive CEP-asymmetry maps from few-cycle MPI of Xe. Experimental data are shown in the top row, and numerical calculations based on spectral interference from the $5P_{3/2}$ ionization continuum are presented in the bottom row. Additionally, polar plots of the CEP-averaged energy-calibrated sections through the *y-z* plane are shown for each asymmetry map. (a) For bandwidth-limited pulses the CEP-dependent oscillations are frequency independent. (b) A down-chirp yields CEP-dependent oscillations of the asymmetry with a linear positive phase shift for increasing energy. The sketch in the middle row illustrates the origin of the linear tilt of the CEP-sensitive interferences: The resulting spectral phase in the overlap regions between multiple ATI channels is locally a linear function, since it is determined by the difference of shifted parabolic phase functions. (c) A third-order polynomial spectral phase function results in CEP-dependent V-shaped structures. In this case, the phase in the overlap region between multiple ATI channels is determined by the difference of two shifted *ungerade* phase functions, leading to a locally *gerade* (parabolic) function, as presented in the sketch in the middle row.

Nth order optical spectrum, with $\omega = (\varepsilon + \text{IP})/\hbar$ and N being the absorbed number of photons to produce the respective threshold or ATI photoelectrons. The center frequency of the Nth order photoelectron spectrum is given by $\omega_N = N\omega_0 - \text{IP}/\hbar$. Since the Nth order nonlinear optical field of a chirped pulse is again a chirped pulse, the spectral phase of its spectrum is also quadratic [35]:

$$\varphi_N^{\text{opt}}(\omega) = \frac{\phi_2}{N}(\omega - N\omega_0)^2. \tag{7}$$

However, according to Eq. (7), the corresponding group delay dispersion is *reduced* by a factor of N. The Nth-order spectral phase of the photoelectrons including the CEP therefore reads

$$\varphi_N(\omega) = N\varphi_{ce} + \frac{\phi_2}{N}(\omega - \omega_N)^2, \tag{8}$$

and analogously the $(N + 1)$-order spectral phase reads

$$\varphi_{N+1}(\omega) = (N + 1)\varphi_{ce} + \frac{\phi_2}{N + 1}(\omega - \omega_{N+1})^2. \tag{9}$$

The phase difference $\Delta\varphi(\omega) = \varphi_{N+1}(\omega) - \varphi_N(\omega)$ between two shifted parabolas is approximately linear, as shown in the sketch in the middle row of Fig. 5(b) on the example of the interference of seventh-order (red dotted line) and 8th-order (blue dashed line) spectra originating from a chirped few-cycle pulse. The slope of the approximately linear phase difference, evaluated at the mean frequency between the Nth- and $(N + 1)$-order spectra, i.e., $\bar{\omega}_N = (\omega_N + \omega_{N+1})/2$, reads

$$\frac{d\Delta\varphi}{d\omega}(\bar{\omega}_N) = \frac{2N + 1}{N(N + 1)}\phi_2(\omega_{N+1} - \omega_N). \quad (10)$$

The chirp parameter of $\phi_2 = -8\,\mathrm{rad/fs^2}$ used in the experiment yields a slope of 5.3 fs at $\bar{\omega}_N$. This calculated value is in accordance with the extracted slope of 5.2 fs of the measured linearly tilted interference pattern (evaluated at $\varepsilon \approx 1.5$ eV) in the asymmetry map in Fig. 5(b). The result for the chirped few-cycle pulse confirms the validity of the simple SI model.

In general, spectral phase functions $\varphi(\omega)$ can be decomposed into their *gerade* and *ungerade* contributions. So far we have described the effect of the chirp, i.e., a *gerade* spectral phase function, on the asymmetry map. Now, we discuss third-order dispersion (TOD) $\varphi(\omega) = \phi_3(\omega - \omega_0)^3$ [35] as a prototype for an *ungerade* spectral phase modulation function. In the case of TOD shown in Fig. 5(c), the interference pattern displays a *gerade* function of energy, resembling a parabolic shape best discernible around 1.8 eV (curved dashed line). To rationalize this pattern, we consider the phase of the Nth-order [and $(N + 1)$-order] spectrum of the laser pulse arising from TOD spectral phase modulation. In general, the higher-order spectra of TOD-modulated pulses are difficult to calculate analytically [46]. However, due to symmetry reasons, the modulated temporal field $E_{\mathrm{mod}}(t)$ is real valued [35] and, therefore, the Nth-order field $E_{\mathrm{mod}}^N(t)$ is also real valued, implying Hermitian symmetry of the corresponding spectrum. The phase of the Nth-order spectrum is thus an *ungerade* function of energy with similar shape. The difference $\Delta\varphi(\omega)$ of the spectral phase of the Nth- and $(N + 1)$-order spectra is obtained by subtracting the two shifted *ungerade* phase functions (centered around ω_N and ω_{N+1}, respectively) yielding a symmetric curve with respect to $\bar{\omega}_N$. As a result, the spectral phase in the overlap region of adjacent ATI channels is locally a *gerade* function of energy with parabolic shape, as illustrated in the sketch in the middle row of Fig. 5(c) on the example of interfering 7th-order (red dotted line) and 8th-order (blue dashed line) spectra generated from a TOD-modulated few-cycle pulse.

In all three cases discussed above, the SI-based simulations shown in the bottom row reproduce well the main features of the asymmetry maps from few-cycle MPI of Xe. Since continuum-continuum interferences originating from the $5P_{3/2}$ and the $5P_{1/2}$ fine-structure components of the Xe^+ ground state, rescattering effects [47], atomic structure, and resonances are not included in the SI model, further observed phase shifts arising in the overlap regions of the threshold and multiple ATI channels at increasing energies are not reproduced by the SI model. Currently, we investigate the origin of those additional phase shifts.

B. Bichromatic ($7\omega : 8\omega$) pulses

Bichromatic multiphoton ionization with a pair of time-delayed bandwidth-limited ($7\omega : 8\omega$) pulses induces controlled interferences of continuum states with opposite parity
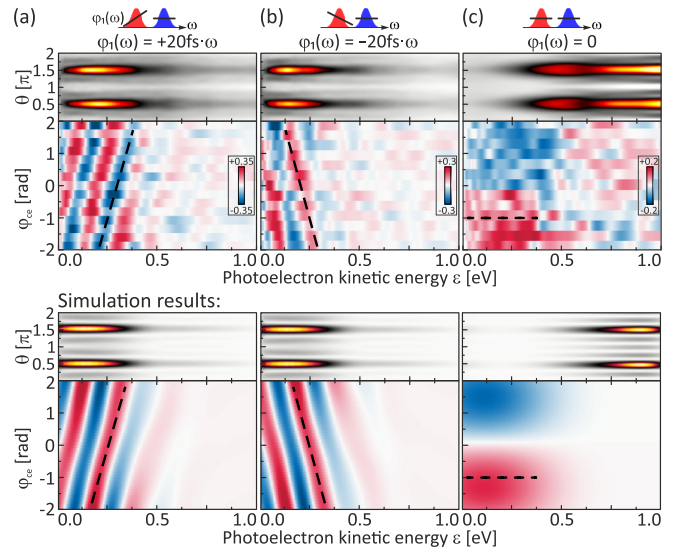

FIG. 6. Phase-sensitive CEP asymmetry maps from bichromatic excitation of Xe. Experimental data are shown in the top row, numerical calculations based on SI from the $5P_{3/2}$ ionization continuum are presented in the bottom row. Additionally, polar plots of the CEP-averaged energy-calibrated sections through the y-z plane are shown for each asymmetry map. (a) A linear spectral phase with positive sign applied to the IR-field yields CEP-dependent oscillations of the asymmetry with a linear positive phase shift for increasing energy. (b) A linear spectral phase with negative sign applied to the IR-field inverts the slope of the observed CEP-oscillations. (c) For time-overlapping bichromatic fields the CEP-dependent oscillations are frequency independent.

in a specific photoelectron kinetic-energy window, as shown schematically in Fig. 1. Because the time delay between the two bandwidth-limited pulses is identical in all nonlinear orders, the spectral phase functions of the spectrally overlapping Nth-order field of the unmodulated reference pulse (blue) and the $(N + 1)$-order field of the time-delayed pulse (red) read

$$\varphi_N(\omega) = N\varphi_{ce}, \quad (11)$$

and

$$\varphi_{N+1}(\omega) = (N + 1)\varphi_{ce} + \omega\tau. \quad (12)$$

Hence, bichromatic time-delayed bandwidth-limited ($7\omega : 8\omega$) pulses introduce a spectral phase difference of

$$\Delta\varphi(\omega) = \varphi_{ce} + \omega\tau \quad (13)$$

in the overlapping region of the nonlinear bichromatic spectrum. The experimental results obtained for bichromatic CEP-control of directional photoemission are depicted in Fig. 6. In the case of time-delayed bichromatic ($7\omega : 8\omega$) pulses with a nonlinear spectral phase of $\Delta\varphi = \varphi_{ce} + 20$ fs ω, corresponding to an initial blue pulse followed by a red pulse, as shown in Fig. 6(a), the 7- vs 8-photon interferences are observed in an energy window around 0.2 eV. The linear slope of the interference pattern is due to the temporal separation of the two colors. These results are qualitatively similar to the above observations on MPI with a chirped few-cycle pulse [see Fig. 5(b)]. The similarity of the CEP-asymmetry maps for chirped MPI in Fig. 5(b) and bichromatic MPI in Fig. 6(a) can be rationalized by realizing that the time-delay

in a bichromatic field corresponds to the group delay in a chirped pulse. In particular, in both cases the blue spectral components interact with Xe atoms earlier than the red ones. In contrast to second-order phase modulation, however, the relative phase between the interfering spectral bands is exactly linear in the bichromatic case, explaining the strictly linear tilt of the $A(\varepsilon, \varphi_{ce})$ interference pattern observed in Fig. 6(a). The energetic fringe separation in the asymmetry map is determined to be $\Delta\varepsilon \approx 0.205$ eV, which corresponds to a time delay of $\tau = h/\Delta\varepsilon = 20.17$ fs. This value is in excellent accordance with the applied time delay of $\tau = 20.0$ fs. Reversal of the pulse ordering (i.e., $\Delta\varphi = \varphi_{ce} - 20$ fs ω, when the red pulse precedes the blue pulse) inverts the sign of the slope, as shown in Fig. 6(b). Here, we extract an energetic fringe separation of $\Delta\varepsilon \approx 0.195$ eV, which corresponds to a time delay of $\tau \approx 21.21$ fs, being in accordance with the applied delay of $\tau = -20.0$ fs. For zero time delay (i.e., $\Delta\varphi = \varphi_{ce}$), shown in Fig. 6(c), additional contributions arise in the photoelectron spectrum at higher kinetic energies due to high-order frequency mixing between both colors [37]. These contributions, located at electron energies $\varepsilon > 0.5$ eV, exhibit only a weak CEP sensitivity since they originate predominantly from processes with the same nonlinearity. Again, the main features of the measured asymmetry maps are reproduced by the SI model displayed in the bottom row. The agreement between experiment and SI model support the proposed physical picture for CEP control of photoemission in the MPI regime.

IV. CONCLUSION AND OUTLOOK

In this paper, we employed spectral amplitude and phase shaping of CEP-stable white light to coherently control lateral asymmetries in the photoelectron momentum distribution from MPI of Xe atoms. Phase-modulated few-cycle pulses and shaper-generated commensurable frequency bichromatic fields with specifically tailored frequency ratio ($7\omega : 8\omega$) were used to control the directional emission of photoelectron wave packets. In the few-cycle case, CEP sensitivity is observed in the energetic overlap region of threshold and multiple ATI channels due to the ultrabroad fundamental spectrum. A physical model based on spectral interference between different ionization pathways was sufficient to reproduce the main features of the CEP asymmetries in the perturbative regime. However, finer features in the photoelectron spectra indicate that the influence of intercontinuum interferences originating from the fine structure components $5P_{3/2}$ and $5P_{1/2}$ of the Xe^+ ground state, atomic resonances and photoelectrons from rescattering need to be included. Due to the multitude of ionization pathways leading to the same photoelectron energy, the interpretation of the interference mechanism in the few-cycle case is generally intricate impeding straightforward coherent control strategies. In contrast, bichromatic fields with a commensurable ($M\omega : N\omega$) frequency ratio, tailored to the actual multiphoton process, allow us to address specific asymmetric final target states via controlled M- vs N-photon multipath interferences. Shaper-generated bichromatic fields provide full optical control over the involved quantum pathways, i.e., over the yield via the bichromatic amplitude ratio and over the phase via the *relative* optical phase and the CEP. Our results show that shaper-generated bichromatic fields with tailored center frequency ratio are a suitable tool to exert control over specific multipath interferences to localize CEP-sensitive asymmetries in a specific photoelectron kinetic-energy window. In fact, pronounced asymmetries of up to 45% (with respect to the CEP average) were observed in the threshold region and could be manipulated with the CEP. By changing the center-frequency ratio, different M- vs N-photon multipath interferences are addressed and, thus, the CEP-sensitive interferences shift into other energy bands of the photoelectron spectrum; for example, from the threshold into the ATI region. So far, bichromatic fields have mostly been generated from superposition of a fundamental laser pulse with a higher-order harmonic. In this scenario, the CEP-dependence of subsequent multiphoton ionization cancels. In this work, we demonstrate that time-delayed bichromatic fields generated by spectral amplitude and phase modulation of CEP-stable WLS using $4f$ polarization shaping techniques preserve the CEP sensitivity in the MPI. By using temporally nonoverlapping bichromatic fields, our results show unambiguously that asymmetries in the photoelectron momentum distribution arise from quantum interference rather than from asymmetries in the optical field. In general, the shaper-based approach allows us to combine control strategies based on bichromatic multipath interference with CEP-sensitive ionization and to simultaneously utilize the full repertoire of femtosecond pulse shaping. By bringing together CEP-sensitive excitation, bichromatic multipath control, and the capabilities of femtosecond pulse shaping, our bichromatic WLS shaping scheme opens new perspectives to a broad range of applications, including high-harmonic generation [48–51], ultrafast multidimensional spectroscopy [52], and high-precision two-color pump-probe experiments with CEP-stable pulses of continuously adjustable frequencies [37]. Currently, we study the creation and CEP control of photoelectron wave packets from MPI of atoms and molecules with *polarization*-tailored bichromatic fields in order to explore the multitude of parameters provided by the bichromatic polarization shaping scheme.

[1] M. Shapiro and P. Brumer, Rep. Prog. Phys. **66**, 859 (2003).

[2] G. G. Paulus, F. Grasbon, H. Walther, P. Villoresi, M. Nisoli, S. Stagira, E. Priori, and S. De Silvestri, Nature (London) **414**, 182 (2001).

[3] M. F. Kling, J. Rauschenberger, A. J. Verhoef, E. Hasovic, T. Uphues, D. B. Milosevic, H. G. Muller, and M. J. J. Vrakking, New J. Phys. **10**, 025024 (2008).

[4] M. J. Abel, T. Pfeifer, A. Jullien, P. M. Nagel, M. J. Bell, D. M. Neumark, and S. R. Leone, J. Phys. B: At., Mol. Opt. Phys. **42**, 075601 (2009).

[5] F. Krausz and M. Ivanov, Rev. Mod. Phys. **81**, 163 (2009).

[6] M. Krüger, M. Schenk, and P. Hommelhoff, Nature (London) **475**, 78 (2011).

[7] B. Piglosiewicz, S. Schmidt, D. J. Park, J. Vogelsang, P. Groß, C. Manzoni, P. Farinello, G. Cerullo, and C. Lienau, Nat. Photon. **8**, 37 (2014).

[8] F. Süßmann, L. Seiffert, S. Zherebtsov, V. Mondes, J. Stierle, M. Arbeiter, J. Plenge, P. Rupp, C. Peltz, A. Kessel, S. A. Trushin, B. Ahn, D. Kim, C. Graf, E. Rühl, M. F. Kling, and T. Fennel, Nat. Commun. **6**, 7944 (2015).

[9] M. F. Ciappina, J. A. Pérez-Hernández, A. S. Landsman, W. A. Okell, S. Zherebtsov, B. Förg, J. Schötz, L. Seiffert, T. Fennel, T. Shaaran, T. Zimmermann, A. Chacón, R. Guichard, A. Zaïr, J. W. G. Tisch, J. P. Marangos, T. Witting, B. Braun, S. A. Maier, L. Roso, M. Krüger, P. Hommelhoff, M. F. Kling, F. Krausz, and M. Lewenstein, Rep. Prog. Phys. **80**, 054401 (2017).

[10] M. F. Kling, C. Siedschlag, A. J. Verhoef, J. I. Khan, M. Schultze, T. Uphues, Y. Ni, M. Uiberacker, M. Drescher, F. Krausz, and M. J. J. Vrakking, Science **312**, 246 (2006).

[11] G. Sansone, F. Kelkensberg, J. F. Pérez-Torres, F. Morales, M. F. Kling, W. Siu, O. Ghafur, P. Johnsson, M. Swoboda, E. Benedetti, F. Ferrari, F. Lépine, J. L. Sanz-Vicario, S. Zherebtsov, I. Znakovskaya, A. L'Huillier, M. Y. Ivanov, F. Martín, and M. J. J. Vrakking, Nature (London) **465**, 763 (2010).

[12] A. S. Alnaser and I. V. Litvinyuk, J. Phys. B: At., Mol. Opt. Phys. **50**, 032002 (2017).

[13] A. Schiffrin, T. Paasch-Colberg, N. Karpowicz, V. Apalkov, D. Gerster, S. Muhlbrandt, M. Korbman, J. Reichert, M. Schultze, S. Holzner, J. V. Barth, R. Kienberger, R. Ernstorfer, V. S. Yakovlev, M. I. Stockman, and F. Krausz, Nature (London) **493**, 70 (2013).

[14] T. Higuchi, C. Heide, K. Ullmann, H. B. Weber, and P. Hommelhoff, Nature (London) **550**, 224 (2017).

[15] H. G. Muller, P. H. Bucksbaum, D. W. Schumacher, and A. Zavriyev, J. Phys. B: At., Mol. Opt. Phys. **23**, 2761 (1990).

[16] Y. Y. Yin, C. Chen, D. S. Elliott, and A. V. Smith, Phys. Rev. Lett. **69**, 2353 (1992).

[17] L. Zhang, X. H. Xie, S. Roither, Y. M. Zhou, P. X. Lu, D. Kartashov, M. Schöffler, D. Shafir, P. B. Corkum, A. Baltuska, A. Staudte, and M. Kitzler, Phys. Rev. Lett. **112**, 193002 (2014).

[18] C. A. Mancuso, D. D. Hickstein, P. Grychtol, R. Knut, O. Kfir, X. M. Tong, F. Dollar, D. Zusin, M. Gopalakrishnan, C. Gentry, E. Turgut, J. L. Ellis, M. C. Chen, A. Fleischer, O. Cohen, H. C. Kapteyn, and M. M. Murnane, Phys. Rev. A **91**, 031402R (2015).

[19] M. R. Thompson, M. K. Thomas, P. F. Taday, J. H. Posthumus, A. J. Langley, L. J. Frasinski, and K. Codling, J. Phys. B: At., Mol. Opt. Phys. **30**, 5755 (1997).

[20] D. Ray, F. He, S. De, W. Cao, H. Mashiko, P. Ranitovic, K. P. Singh, I. Znakovskaya, U. Thumm, G. G. Paulus, M. F. Kling, I. V. Litvinyuk, and C. L. Cocke, Phys. Rev. Lett. **103**, 223201 (2009).

[21] X. Gong, P. He, Q. Song, Q. Ji, H. Pan, J. Ding, F. He, H. Zeng, and J. Wu, Phys. Rev. Lett. **113**, 203001 (2014).

[22] M. Förster, T. Paschen, M. Krüger, C. Lemell, G. Wachter, F. Libisch, T. Madlener, J. Burgdörfer, and P. Hommelhoff, Phys. Rev. Lett. **117**, 217601 (2016).

[23] J. Passig, S. Zherebtsov, R. Irsig, M. Arbeiter, C. Peltz, S. Göde, S. Skruszewicz, K. H. Meiwes-Broer, J. Tiggesbäumker, M. F. Kling, and T. Fennel, Nat. Commun. **8**, 1181 (2017).

[24] E. Dupont, P. B. Corkum, H. C. Liu, M. Buchanan, and Z. R. Wasilewski, Phys. Rev. Lett. **74**, 3596 (1995).

[25] L. Costa, M. Betz, M. Spasenovic, A. D. Bristow, and H. M. Van Driel, Nat. Phys. **3**, 632 (2007).

[26] J. Güdde, M. Rohleder, T. Meier, S. W. Koch, and U. Höfer, Science **318**, 1287 (2007).

[27] T. Brabec and F. Krausz, Rev. Mod. Phys. **72**, 545 (2000).

[28] M. Abel, D. M. Neumark, S. R. Leone, and T. Pfeifer, Laser Photonics Rev. **5**, 352 (2011).

[29] T. Brixner and G. Gerber, Opt. Lett. **26**, 557 (2001).

[30] A. M. Weiner, Rev. Sci. Instrum. **71**, 1929 (2000).

[31] S. Kerbstadt, L. Englert, T. Bayer, and M. Wollenhaupt, J. Mod. Opt. **64**, 1010 (2017).

[32] S. Kerbstadt, D. Timmer, L. Englert, T. Bayer, and M. Wollenhaupt, Opt. Express **25**, 12518 (2017).

[33] A. M. Weiner, Opt. Commun. **284**, 3669 (2011).

[34] A. Monmayrant, S. Weber, and B. Chatel, J. Phys. B: At., Mol. Opt. Phys. **43**, 103001 (2010).

[35] M. Wollenhaupt, A. Assion, and T. Baumert, in *Springer Handbook of Lasers and Optics* (Springer, Berlin, Heidelberg, 2012), Vol. 2.

[36] G. Cerullo, A. Baltuska, O. D. Mucke, and C. Vozzi, Laser Photonics Rev. **5**, 323 (2011).

[37] S. Kerbstadt, D. Pengel, D. Johannmeyer, L. Englert, T. Bayer, and M. Wollenhaupt, New J. Phys. **19**, 103017 (2017).

[38] S. Luo, M. Li, H. Xie, P. Zhang, S. Xu, Y. Li, Y. Zhou, P. Lan, and P. Lu, Phys. Rev. A **96**, 023417 (2017).

[39] T. Baumert, T. Brixner, V. Seyfried, M. Strehle, and G. Gerber, Appl. Phys. B: Lasers Opt. **65**, 779 (1997).

[40] D. Yelin, D. Meshulach, and Y. Silberberg, Opt. Lett. **22**, 1793 (1997).

[41] M. Wollenhaupt, T. Bayer, and T. Baumert, Control of ultrafast electron dynamics with shaped femtosecond laser pulses: From atoms to solids, in *Ultrafast Dynamics Driven by Intense Light Pulses*, edited by S. Gräfe and M. Kitzler (Springer, Cham, Heidelberg, New York, Dordrecht, London, 2015), Book section4, pp. 63–122.

[42] A. T. J. B. Eppink and D. H. Parker, Rev. Sci. Instrum. **68**, 3477 (1997).

[43] G. A. Garcia, L. Nahon, and I. Powis, Rev. Sci. Instrum. **75**, 4989 (2004).

[44] A. Wituschek, J. von Vangerow, J. Grzesiak, F. Stienkemeier, and M. Mudrich, Rev. Sci. Instrum. **87**, 083105 (2016).

[45] A. Galler and T. Feurer, Appl. Phys. B: Lasers Opt. **90**, 427 (2008).

[46] M. Ruge, R. Wilcken, M. Wollenhaupt, A. Horn, and T. Baumert, J. Phys. Chem. C **117**, 11780 (2013).

[47] D. W. Schumacher, F. Weihe, H. G. Muller, and P. H. Bucksbaum, Phys. Rev. Lett. **73**, 1344 (1994).

[48] S. Long, W. Becker, and J. K. McIver, Phys. Rev. A **52**, 2262 (1995).

[49] D. B. Milosevic and W. Becker, Phys. Rev. A **62**, 011403R (2000).

[50] A. Fleischer, O. Kfir, T. Diskin, P. Sidorenko, and O. Cohen, Nat. Photonics **8**, 543 (2014).

[51] O. Kfir, P. Grychtol, E. Turgut, R. Knut, D. Zusin, D. Popmintchev, T. Popmintchev, H. Nembach, J. M. Shaw, A. Fleischer, H. Kapteyn, M. Murnane, and O. Cohen, Nat. Photonics **9**, 99 (2015).

[52] D. M. Jonas, Annu. Rev. Phys. Chem. **54**, 425 (2003).